Evaluation of CFD methods for transport aircraft high lift systems

R. Rudnik
DLR, German Aerospace Center
Institute of Aerodynamics and Flow Technologies, Braunschweig, Germany

P. Eliasson
FOI, Swedish Defense Research Agency
Aeronautics Division, Stockholm, Sweden

J. Perraud
ONERA, Office National d'Etudes et de Recherches Aerospatiales
CERT/DMAE, Toulouse, France

ABSTRACT

Major results and findings of the numerical work package of the European high lift programme EUROLIFT are outlined. The main objective of these studies is to validate and test numerical methods for the prediction of high lift flows for transport aircraft configurations. The activities comprise the assessment of current CFD methods for 3D flows, evaluation of means for code improvement, and transition prediction. All aspects are especially devoted to high lift flow problems. A general capability to predict maximum lift on a simplified wing/fuselage high lift configuration is demonstrated by a variety of different numerical approaches. In general, major shortcomings are the reliability and the accurate simulation of large separation areas and the turn-around time to compute 3D lift polars. Advanced turbulence modelling and numerical solver features, such as the preconditioning technique, show a potential to overcome these deficiencies. Promising results with respect to transition prediction were obtained on a swept high lift wing using a database method. The results obtained in the numerical activities represent major ingredients on the way to a consistent numerical approach for the simulation of transport aircraft high lift configurations including all maximum lift determining effects.

NOMENCLATURE

F non-dimensional frequency of instability, $F = \frac{2\pi f \nu}{U_e^2}$

H_1 incompressible shape factor, ratio of the displacement thickness δ_1 to the momentum thickness θ, $H_1 = \frac{\delta_1}{\theta}$

P_i parameter for the crossflow database model $P_i = y_i \left(\frac{\partial U}{\partial y} \right)_i$

K acceleration parameter, $K = \frac{\nu}{U_e^2} \frac{\partial U_e}{\partial x}$

R attachment line contamination Reynolds number, $\bar{R} = W_e \Big/ \sqrt{\nu \left(\frac{\partial U_e}{\partial X} \right)_{X_a}}$

$\bar{R}$. height of the inflection point on the boundary layer profile

U_e chord wise velocity component, in x direction

W_e span wise velocity component, in z direction

φ model sweep angle

ν kinematic viscosity

α model incidence

σ growth rate of instabilities

1.0 INTRODUCTION

The numerical simulation of the flow field around high lift configurations based on methods for the solution of the Reynolds-averaged Navier-Stokes (RANS) equations has made significant progress during the last decade[1]. Until the beginning of the EUROLIFT project in early 2000, most of the European activities had been devoted to two-dimensional computations[2]. Thus, the extension to 3D high lift applications was the consequent next step to be made. Despite the existence of the comprehensive experimental database of the GARTEUR group[3], the limited access of the GARTEUR data and the need for a state-of-the-art experimental database stimulated

Paper No. 2895. Manuscript received 7 May 2004, revised version received 27 October 2004, accepted 8 November 2004.

https://doi.org/10.1017/S0001924000000555 Published online by Cambridge University Press

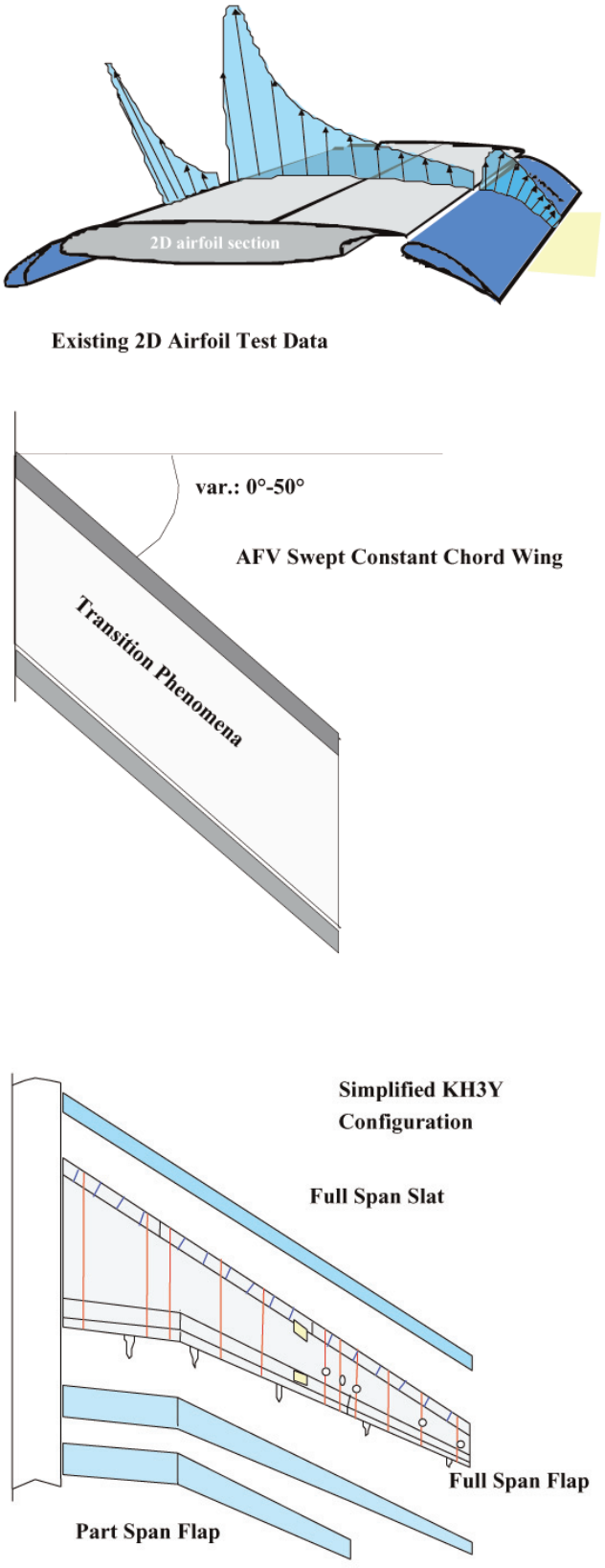


Figure 1. Overview about the configurations treated in the numerical work package of EUROLIFT.

the launch of the EUROLIFT high lift programme[4], funded by the EC as part of the Fifth Framework program. In contrast to the GARTEUR studies, a close coupling and harmonisation of the experimental and numerical activities within one project phase is attempted in EUROLIFT. This is considered essential, as the lack of input of the numerical requirements in the definition of validation experiments and the direct access and insight to the 'production' of experimental data has often been a shortcoming for validation exercises.

The EUROLIFT code validation activities have been grouped in the work packages *Validation Experiments and Flow Phenomena*, WP1, and *CFD Assessment and Improvement*, WP2. The important relation to industrial applications is considered in a third work package entitled *Verification and Application of High Reynolds number Testing*, WP3. The understanding and correct simulation of Reynolds number scaling effects is one of the most important challenges of today's high lift system design. Within EUROLIFT, the required experimental data up to flight Reynolds number are provided by tests in the European Transonic Wind Tunnel (ETW) in Cologne. Complementary to tests in the Airbus-Deutschland low speed facility LSWT in Bremen, the high Reynolds number tests contribute to the completion of the validation data in WP1, as well as to studies on a novel high lift system under investigation at Airbus-Deutschland. The experiments for the study of transition phenomena have been carried out in the French F1 facility of ONERA in le Fauga.

Concerning the configurations considered in work package 2, a step by step complexity increase is followed in the project, as sketched in Fig. 1. The main configuration is the KH3Y wing/fuselage configuration, representing an Airbus-like generic development model. This model is investigated in take-off and landing settings and in full-span and part-span flap configurations. The transition investigations were carried out on the constant chord variable sweep high lift wing AFV. The code improvement investigations basically make use of existing 2D experimental data, taken from GARTEUR research activities and from a national German high lift programme. Thus, no 2D tests were conducted within EUROLIFT.

The present contribution describes the activities in the numerical work package of EUROLIFT[5]. An overview about the achievements is given by selected results of the three tasks that form the numerical activities. These tasks are:

- CFD assessment for high lift application,
- CFD improvement for high lift application,
- Transition prediction for high lift application.

Main results in these three research areas are outlined.

2.0 ASSESSMENT OF CFD METHODS

The major objective of the code assessment task is the application of several numerical Navier-Stokes methods for the simulation of maximum lift on a 3D-transport aircraft configuration with deployed high lift devices. A total of ten different partners contributed to this activity. An overview about the involved partner as well as their numerical methods is given in Ref. (5). Basically, the methods in use are divided into those, which work on block-structured grids, and those, which work on (hybrid) unstructured grids. With the exception of Dassault Aviation, all methods are based on a finite volume formulation of the governing equations. The code of Dassault Aviation uses a finite element formulation on purely unstructured grids.

One of the main activities in the present task is the comparison of the structured and the hybrid unstructured grid approaches for a selected test case. This benchmark case is given by the full span flap and slat KH3Y configuration in take-off setting for low Reynolds number conditions. In order to allow each partner to compute this case, an upper point number limit of 3m grid points had to be met for

https://doi.org/10.1017/S0001924000000555 Published online by Cambridge University Press

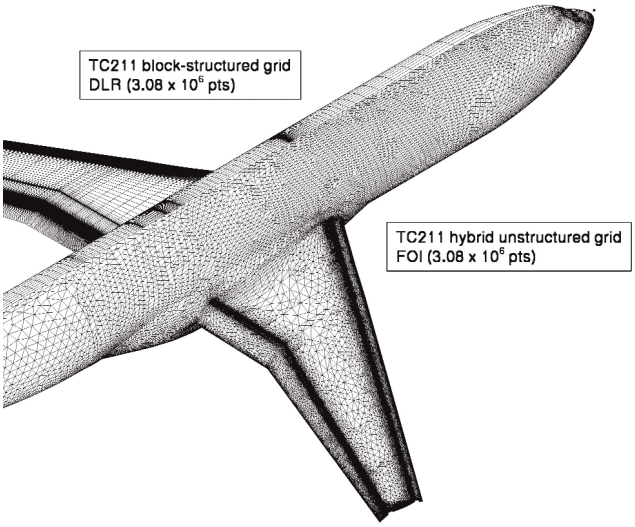


Figure 2. Mandatory grids for KH3Y configuration.

both mandatory grids. Figure 2 shows the resulting block-structured grid of DLR, consisting of 49 blocks (left hand side), and the hybrid unstructured counterpart of FOI (right hand side). The near wall area of the hybrid unstructured grids is resolved with prismatic elements. Although the total grid point number is nearly identical, it has to be kept in mind that the number of points along the aerodynamic surfaces of the unstructured grid is nearly one order of magnitude higher than that of the block-structured one. On the other hand, the resolution normal to the aerodynamic surfaces is higher for the block-structured grid. Consequently, there are considerable differences in local grid resolution. The basis for the comparison is therefore a best practice approach for both grid types. A representative selection of polar results is depicted in Fig. 3. The polar computations are characterised by five to ten single 3D-flow field computations for each contribution. A fair agreement is obtained between RANS computations and LSWT experiments in the linear range of the polar. Lift is generally underestimated because of two main reasons. First, fully turbulent conditions are assumed for all computational results of the benchmark case. Although transition locations were measured by hot films and infrared pictures, the required complete set of transition locations on all elements for the different flow conditions was not available when the benchmark computations started. Second, the comparatively coarse grids also contribute to the lift underestimation. Both reasons, neglecting laminar flow areas as well as a coarse streamwise resolution, lead to an underprediction of the leading-edge suctions peaks. Accordingly, the total drag is overpredicted. The scatter of results increases at maximum lift conditions from seven lift counts at an angle-of-attack of 7° to 16 lift counts for the experimental maximum lift incidence. All RANS methods predict a maximum lift, but especially the scatter for the corresponding angle-of-attack is quite large. As a typical example the computed stall mechanism may be highlighted referring to the result of the DLR FLOWer code on the block-structured grid. For an angle-of-attack of 24°, beyond maximum lift, the wall streamlines indicate a strong slat separation as well as a separation at the trailing edge of the fixed wing close to the kink, see Fig. 4. The slat separation is found in every computed result with varying intensity and extension. It is confirmed by the low Reynolds number experiments in the LSWT, based on local force analysis. In general, both the block-structured and the unstructured methods reveal a comparable simulation quality with similar maximum lift behaviour.

Although at present a more efficient grid point distribution is

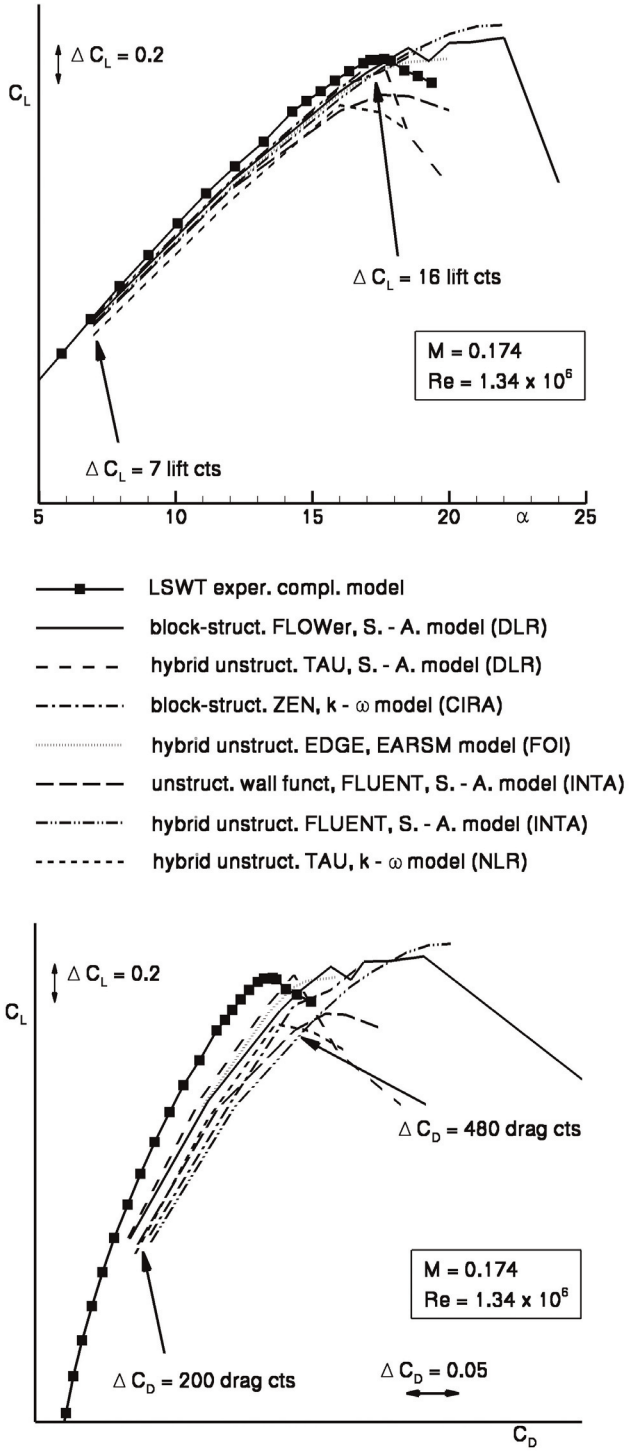


Figure 3. Lift and drag polar for low Reynolds-number conditions.

feasible using the block-structured grid generation, the required user effort is considerably higher than that for the hybrid unstructured grids. The use of the Chimera technique has the potential to reduce this effort. At the same time the configuration complexity may be more easily increased. The application of the Chimera technique to a full three-dimensional high lift configuration has been investigated

https://doi.org/10.1017/S0001924000000555 Published online by Cambridge University Press

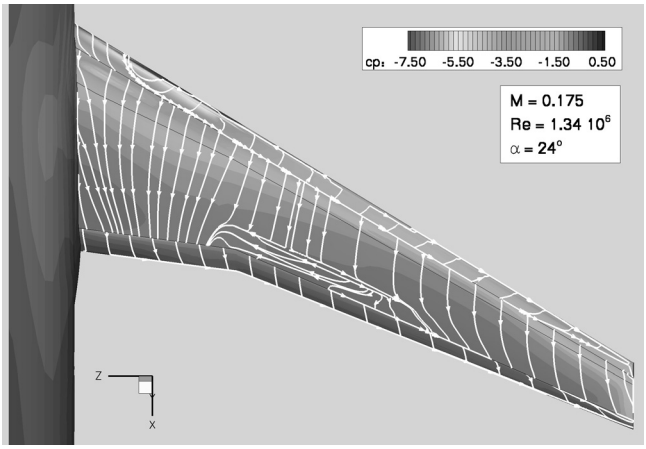


Figure 4. Isobars and wall streamlines beyond maximum lift for the DLR block-structured computation.



Figure 7. KH3Y part span flap configuration.

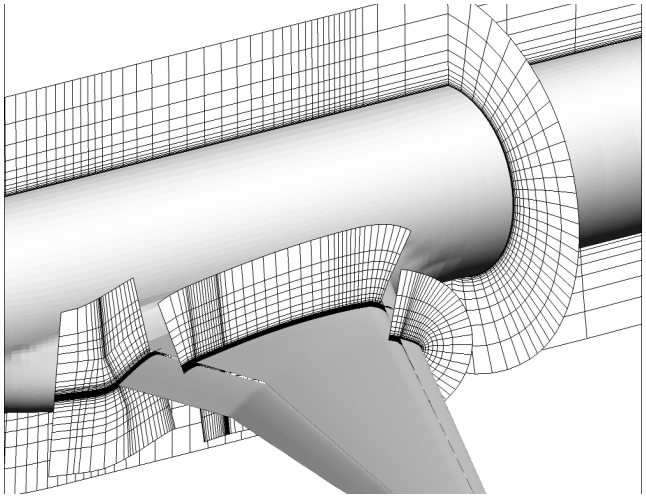


Figure 5. 3D Chimera grid for KH3Y configuration.

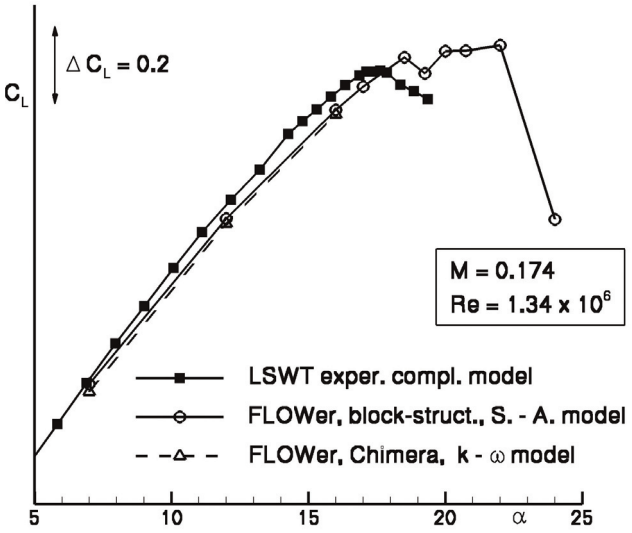


Figure 6. Lift polar for block-structured *vs* Chimera approach.

based on the structured method of DLR[6]. Cutting planes of the chimera grid for the KH3Y take-off configuration are shown in Fig. 5. The grid consists of 3·9m grid points in 333 blocks. So the grid point number is roughly 30% higher than that of the block-structured grid, which is taken as a starting point for the Chimera grid. The Chimera process and the generation of the Cartesian background grids are widely automated. The *k*-ω model was selected, due to its fully local formulation, for the computations with the FLOWer code. The computational results in the linear lift range are compared to the lift polar of the block-structured computations in Fig. 6. Despite the different turbulence model and the finer grid, the total lift agrees quite well with the baseline FLOWer computations for the three considered incidences. Nevertheless, the Chimera technique still needs progress with respect to automation and efficiency. Questions relative to its improvements are discussed in Section 3 'Improvements of CFD Methods'.

After the benchmark study, investigations on the simulation of Reynolds number effects and complexity increase have been carried out. As a moderate complexity increase, a part span flap configuration was computed in take-off setting. The lateral extension of the flap is reduced to about 73% of the half span, see Fig. 7. The hybrid unstructured grid is generated by FOI and contains 4·5m grid points. The computed and measured low Reynolds number lift curves are shown in Fig. 8. Computations have been carried out using the DLR TAU code and the Spalart-Allmaras turbulence model with Edwards-modification[7]. The nearly constant lift loss of the part span flap model of about 10% at a given incidence is quite well reproduced by the numerical simulation. In agreement with the experiments, the lift loss is maintained throughout the maximum lift regime. In contrast to this, the simulated decrease of maximum lift due to the reduced flap extension is significantly underpredicted. The reason for this miss-prediction is the underestimation of the trailing edge separation in the outboard portion of the wing in the computational results.

An important item of the part span flap study is the ability of the numerical method to capture the drag reduction of the extended or full span flap configuration for the same total lift. This drag issue is most relevant for the take-off performance in the second segment of the climb phase. Analysing the corresponding drag polars in Fig. 9 reveals that the drag reduction of about 20 drag counts in the lower lift range is reasonably captured by the computations. On the other hand, the evaluation of the computed results has to be regarded with

https://doi.org/10.1017/S0001924000000555 Published online by Cambridge University Press

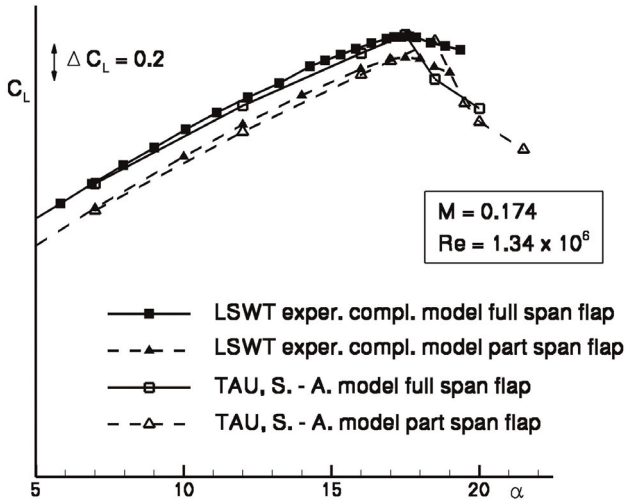


Figure 8. Lift polar for extend full and part span flap configuration.

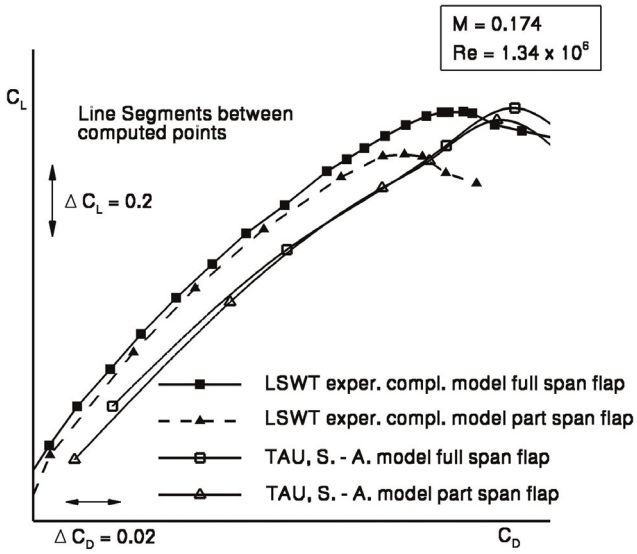


Figure 9. Drag increment due to extended flap concept.

caution due to the rather limited number of computed polar points. Therefore the assessment of the drag difference at higher angles of attack is quite difficult and needs further investigations.

3.0 IMPROVEMENTS OF CFD METHODS

The flow around high lift systems is characterised by a number of complex phenomena that often interact. The local Mach number is varying widely; there are re-circulation zones in the coves, flow separation, wake and boundary confluence, transition etc. The design of high lift configurations requires reliable CFD prediction tools of these phenomena. This refers to the efficiency of the tools, their prediction capability as well as their accuracy.

Within the CFD improvement activity, the work is divided in three subtasks including:

- Grid generation algorithms
- Turbulence modelling
- Solver efficiency and accuracy.

Table 1
Summary of 2D grids used for A310 test case

Partner	Case	No of nodes	Type of grid
DLR	A310	80,000	Structured
DLR	A310	330,000	Structured
Alenia	A310	35,000	Unstructured
ONERA	A310	100,000	Overlapping, block struct.

In summary, the work for turbulence modelling is directed towards implementation and extension of EARSM[8] (explicit algebraic Reynolds stress models), but also non-linear eddy viscosity models and the evaluation of a full Reynolds stress model (RSM) in a commercial flow solver. In the solver efficiency subtask, low speed preconditioning is the main contribution. Grid generation deals primarily with several advanced grid generation algorithms for unstructured grids, overlapping grids and grid adaptation techniques.

The first part of the project was devoted to implementation of algorithms followed by a preliminary and final validation in the second part. Any improvement should be compared against the assessment carried out in the first half of the project. A major focus of the CFD improvement work has been to separate the influences of turbulence modelling, grid resolution, and solver accuracy to assess the shortcomings of simulation and direct improvement activities. Another important outcome of the CFD improvement is to see how well the computed results compare on the different grid types used, structured multi-block, unstructured hybrid and overlapping structured block grids.

The focus in this paper will be on the turbulence modelling for high lift flow phenomena, which have been successfully predicted, some phenomena that still are not well predicted and grid resolution issues. A more detailed overview of the CFD improvements in EUROLIFT is given in Ref. 9.

3.1 Test cases

Although the main focus of EUROLIFT lies on 3D configurations, the focus for the CFD improvements is on 2D three-element configurations due to the reduced effort to study grid resolution aspects, grid custering strategies, turbulence model performance, solver efficiency and accuracy aspects. The 2D test cases are the same as those used in the assessment activity, one being the A310 three-element landing configuration numerically and experimentally evaluated in GARTEUR. The second test case is the H8Y three-element take-off configuration experimentally evaluated in the national German high lift programme[10] and related to the 3D KH3Y model, being the main EUROLIFT configuration.

The grid generation for these configurations was carried out as part of the initial assessment and with the new tools developed in the CFD improvement task. Structured, unstructured and overlapping grids were generated with up to more than 300,000 grid nodes. The grids used for the A310 three-element aerofoil are summarised in Table 1.

The free stream conditions for the 2D cases are

- A310 landing configuration:
  $M = 0{\cdot}22$, $Re = 4{\cdot}1 \times 10^6$
- H8Y take-off configuration:
  $M = 0{\cdot}20$, $Re = 9 \times 10^6$

The H8Y calculations are carried out fully turbulent. The A310 case is computed with transition locations derived from boundary layer calculations.

https://doi.org/10.1017/S0001924000000555 Published online by Cambridge University Press

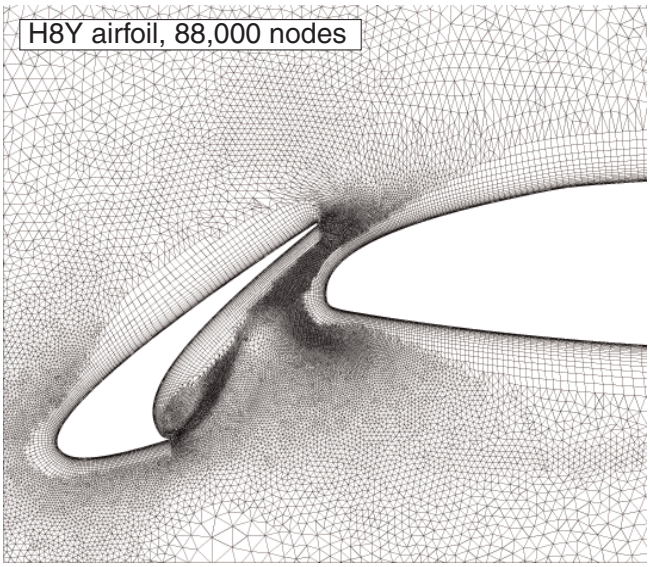


Figure 10. Unstructured grid at the slat of H8Y aerofoil (FOI).

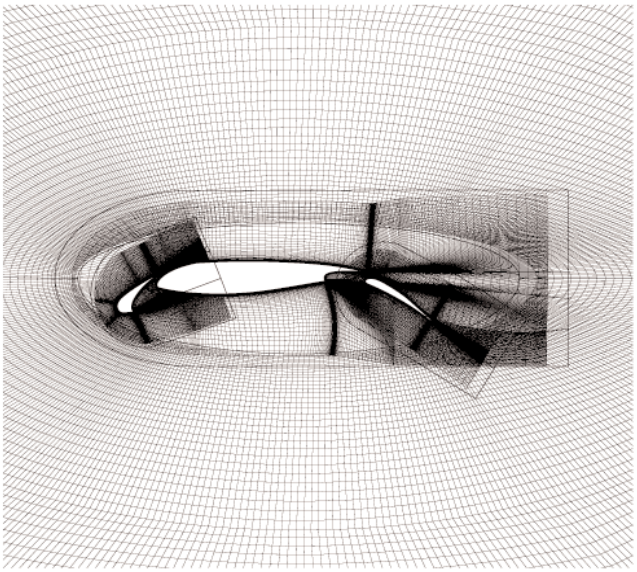


Figure 12. Chimera grid for H8Y three-element aerofoil.

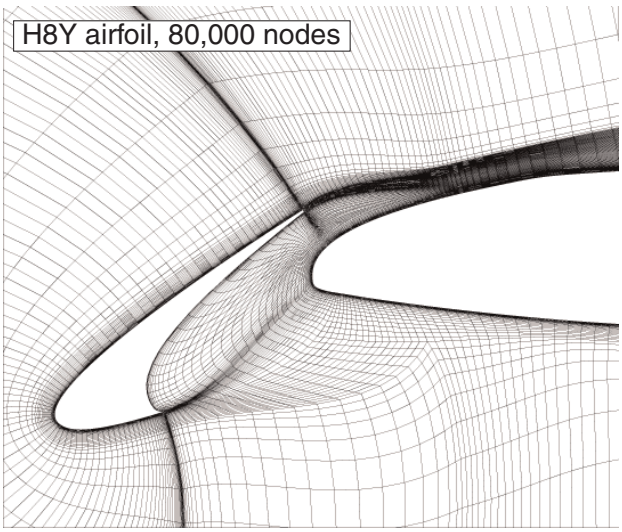


Figure 11. Block-structured grid at the slat of the H8Y aerofoil.

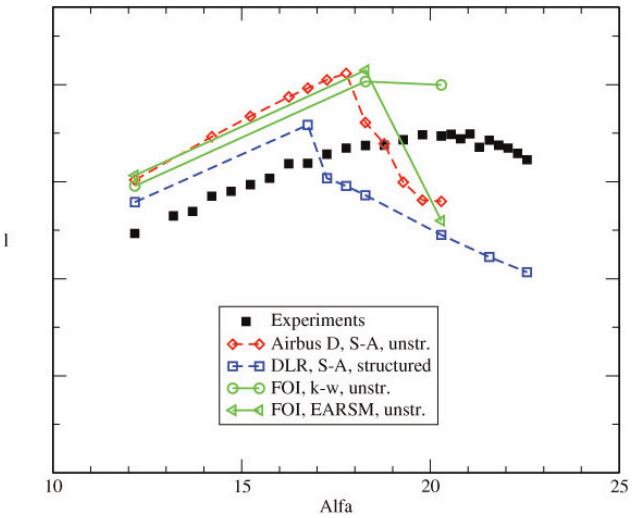


Figure 13. Lift polar for the H8Y aerofoil.

3.2 Results on grid generation

In the grid generation subtask, the main development is directed to deal with complex geometries for unstructured grids. One example is the introduction of variable numbers of prismatic elements in the boundary layer as displayed for an adapted grid for H8Y. A close up at the forward slat element of this grid is displayed in Fig. 10, and the corresponding block structured grid is displayed in Fig. 11. Another example of a grid generation activity is the Chimera grid generated by ONERA for A310 aerofoil, which is shown in Fig. 12. Four overlapping block structured grids are used, one grid for the far field, the main body, the slat and the flap.

3.3 Results on turbulence modelling

During the initial assessment, the computed results for the H8Y aerofoil turned out to reproduce the experimental results rather poorly close to maximum lift for almost all partners. An example of a lift polar for H8Y can be seen in Fig. 13. The experimental lift values have been obtained by numerical integration of the surface pressure distribution, because no direct force measurement has been carried out in the 2D experiments in the HST facility in Amsterdam. Due to a smaller number of sampling points the surface integration tends to underestimate the total lift compared to the direct lift determination. The numerical results over predict experimental lift values at lower angles of attack. More critical, though, is that the experimental stall behaviour is in general not reproduced by the numerical predictions. A premature stall is computed, characterised by a separated region on the slat upper surface causing a drastic reduction of lift. This behaviour is the same for almost all partners, grids and turbulence models with very few exceptions. An investigation with prescribing transition on the slat based on linear stability analysis was also carried out but did not result in any substantial differences. This detailed investigation as part of the numerical assessment is described in Ref. 11.

https://doi.org/10.1017/S0001924000000555 Published online by Cambridge University Press

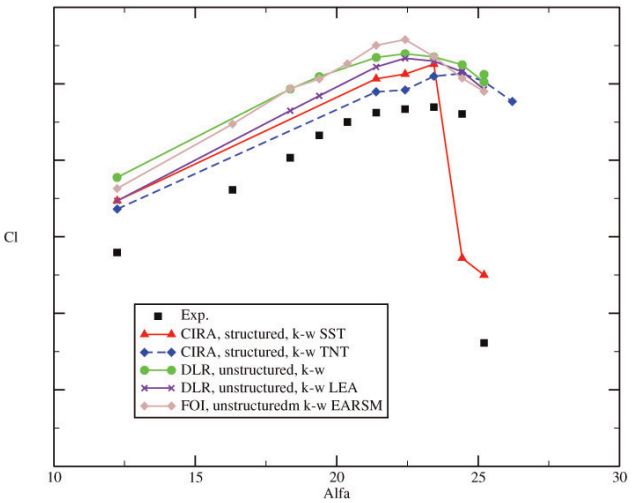


Figure 14. Lift polar for the A310 aerofoil.

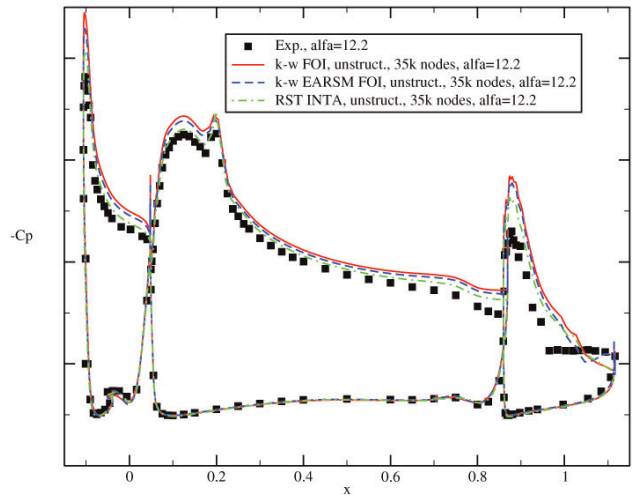


Figure 15. C_p distribution, α =12·2°, for the A310 aerofoil. Eddy viscosity model, EARSM and RST.

Due to the uncertainties and open questions for the H8Y model, the focus in the CFD improvement was shifted to the GARTEUR A310 configuration. For this case a comprehensive experimental database exists for validation purposes. The lift polars from several partners are plotted in Fig.14 and compared to experimental results of the NLR HST wind tunnel. The figure includes results obtained with different turbulence models as well as structured and unstructured grids of different densities. All partners predict the maximum lift at approximately the right angle-of-attack. The lift is still slightly overpredicted compared to experimental data. Again, this is not critical and is partly due to different integration techniques of experimental and numerical data. More important though is that the maximum lift regime is correctly reproduced. There are in general small differences between the predicted results. The results on structured and unstructured grids are in good agreement. The main differences come from the use of different turbulence models. All models in Fig. 14 are based on the standard k-ω model. The model extensions are TNT, SST extensions, a linear EARSM (LEA) extension and full non-linear EARSM extension. There is no indication from this figure that the EARSM leads to an improved prediction. The lift is still over predicted, especially at the lower angles, and the stall

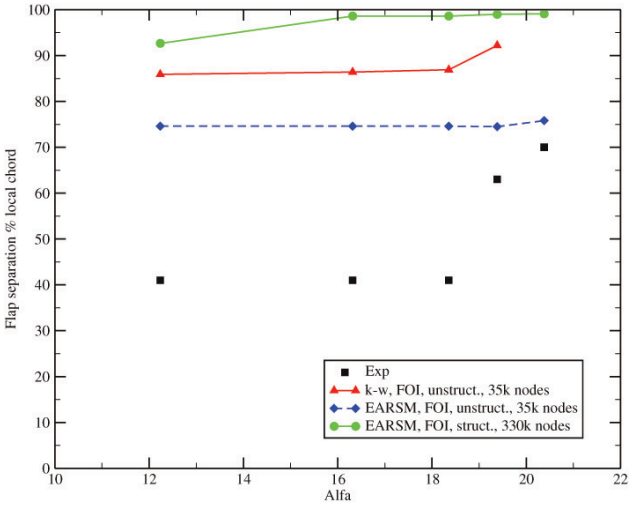


Figure 16. Starting point of flap separation in %local chord for the A310 aerofoil.

observed in experiments at the highest angle-of-attack is not reproduced numerically by EARSM coupled to the k-ω model.

At the lowest angle-of-attack there is a typical flap separation due to its high deflection in landing configuration. All attempts to quantitatively predict this separation failed in the initial assessment using linear eddy viscosity models, only a very small separation was predicted, if any and too far down stream. One objective was to see if more advanced turbulence models could improve these predictions. In Fig. 15 the pressure distributions are displayed using a standard k-ω model, an EARSM extension of a k-ω model and a full Reynolds Stress Model (RSM) implemented in the commercial solver Fluent. None of the models manages to accurately predict the flap separation. EARSM and RSM predict a small separation at the very rear part of the flap, far downstream of the experimental location. Although the separation is not correctly predicted, the suction pressure distribution is brought closer to experimental values as the turbulence modelling complexity is increased. As a result, the overprediction of lift is reduced.

In Fig. 16 the start position of the flap separation in percentage of local chord is shown for the lower angles-of-attack using the EARSM model on an unstructured grid (35,000 nodes), compared to a strongly refined structured grid (330,000 nodes). As a reference, results with the standard k-ω model are displayed as well. The starting position of the experimental separation has been estimated from the beginning of the flat area in the experimental pressure distribution. It can be seen that, using the same grid, with the EARSM extension the point of separation moves in the direction of the experimental location compared to the k-ω model results. However, as the grid is refined, the separated region becomes even smaller moving the solution further away from the experimental results. The delayed prediction of separation is thus not attributed to the grid resolution. The answer may possibly be found in the RANS modelling approach and could perhaps be resolved with a hybrid RANS/LES or pure LES approach. There may also be 3D effects or other effects from the experimental set-up, which have not been accounted for.

In Fig. 14 it can be seen that most partners do not predict the strong breakdown beyond maximum lift. Only the k-ω SST model predicts this feature but ahead of the experimental angle-of-attack. One partner has managed to predict the stalled flow very well at the highest angle-of-attack using the EARSM extension coupled to the k-ω equations. The flow was not completely steady and hence the calculations were carried out in unsteady mode, although the unsteady effects were marginal. The pressure distribution of this

https://doi.org/10.1017/S0001924000000555 Published online by Cambridge University Press

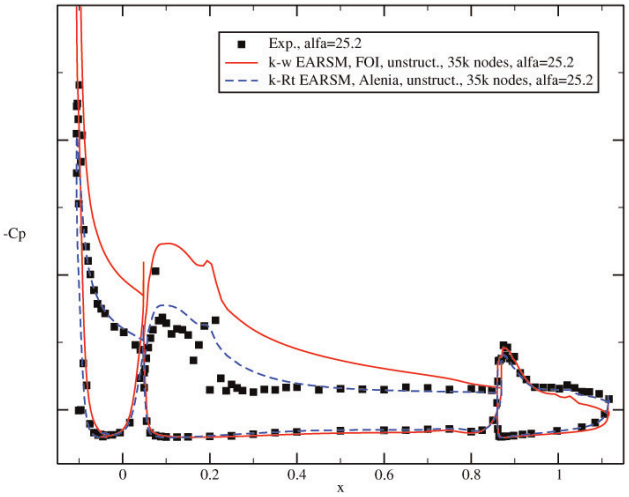


Figure 17. C_p distribution, $\alpha = 25{\cdot}2°$, A310 aerofoil. EARSM with length scale based on ω and R_t.

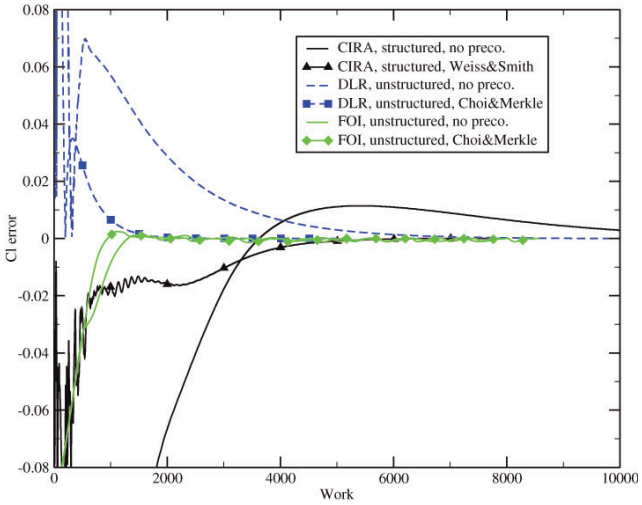


Figure 18. Convergence of error of lift with and without low speed preconditioning, A310 aerofoil.

calculation and the EARSM calculation coupled to the k-ω model can be seen in Fig. 17. A large part of the flow on both the flap and main element is separated, indicating a trailing edge type of stall. This stalled flow could not be predicted with a linear k-R_t eddy viscosity model by the same partner. This is a good demonstration of an improvement due to a higher and more sophisticated modelling level. Note that the results with EARSM extension coupled to the k-ω results do not predict stall. Hence it is not sufficient to base the analysis on the EARSM extension alone. The different length scale equations (here based on R_t or ω) have also to be taken into account. This will be an area for future research.

Although not demonstrated here it should be noted that the results obtained with overlapping Chimera grids have shown satisfactory agreement with results obtained on block structured and unstructured grids. The main difference between all numerical results is due to turbulence modelling and not to the different grid types, provided the grid is well resolved.

The fact that high lift flows contain both low speed and transonic regions reduces the efficiency of the solver due to slow convergence rates to steady state. A remedy to this is low speed local preconditioning methods with a potential to improve both efficiency as well as accuracy of low speed computations with compressible codes. In Fig. 18 the convergence of the error to the integrated lift without and with preconditioning methods by Choi and Merkle[12] and Weiss and Smith[13] is displayed for three partners. The gain using preconditioning can clearly be seen. The overall computational benefit from low speed preconditioning obtained by all partners varies from 33% to 70% depending on the preconditioning method and implementation details.

4.0 TRANSITION IN HIGH LIFT

The laminar-turbulent transition on high lift configurations is an important topic related to the prediction of maximum lift. Reliable determination of maximum lift is best obtained in wind tunnel experiments, as especially 3D codes do not yet guarantee sufficient accuracy and turn-around-time. However, most of the high lift tests are carried out at sub-scale conditions, and aircraft performances are derived by extrapolation to flight Reynolds number. Such extrapolation requires a good understanding of the transition process, and its change with Reynolds number.

Transition to turbulence may occur, on profiles at large angle of incidence, in several distinct ways. At low Reynolds numbers, crossflow (CF) instabilities in the accelerated flow region are not strong enough to cause transition. The flow remains laminar down to the velocity peak, and quite often, a short bubble transition is observed. Increasing the Reynolds number causes a rise of the amplification of the CF instabilities, until transition occurs upstream of the previous separation location. At even larger Reynolds number, attachment line contamination will occur, sometimes followed by relaminarisation. So called adverse Reynolds number effects are strongly related to changes in the transition process from low to high Reynolds numbers.

Increasing the capacity of computational tools requires validation of models for aircraft wings in cruise conditions (high Reynolds numbers) that were developed during the last years. For transition controlled by boundary-layer instabilities, these methods are based on the linear stability theory, either in its local (Orr-Sommerfeld) or non-local (parabolised stability equations) formulation. Reduction of turn-around-time in transition prediction is also a major goal, as stability computations are difficult and time consuming. Introduction of simplified methods, which require a very small fraction of the time used in classical stability work, is a promising development. ONERA has developed such simplified methods[14,15], especially in past EC programmes. In the course of EUROLIFT, they were distributed to the project partners involved in the transition prediction activity for implementation in various codes and validation. Other phenomena to be predicted are short bubble transition, attachment line contamination and relaminarisation. For these, validation of existing methods was also required. Partners involved in this activity were Airbus Deutschland, CASA & INTA of Spain, CIRA (Italy), and FOI (Sweden).

4.1 Strategy of the EUROLIFT transition activity

The transition prediction work consisted in a step by step validation of tools common to the project partners. They are implemented into each partner's flow solver, and aiming at predicting contamination, separation, transition and relaminarisation.

Despite the general objective of a RANS based prediction method for high lift, it was shown at the start of the project that RANS computations of the viscous wall regions could not reasonably provide the precision required for stability calculation and transition prediction. Artificial viscosity allowing rapid convergence and

https://doi.org/10.1017/S0001924000000555 Published online by Cambridge University Press

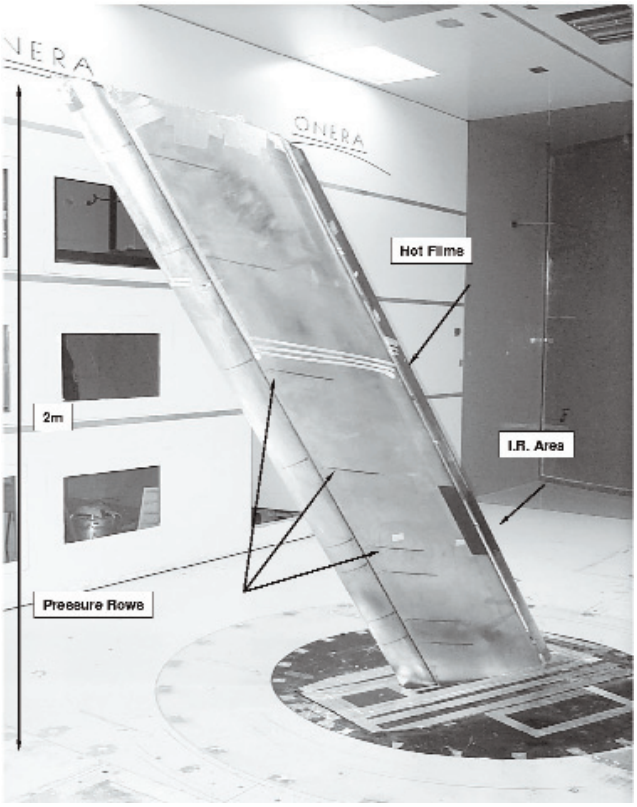


Figure 19. AFV model in F1 ONERA wind tunnel.

numerical stability is not compatible with precise computation of laminar boundary layers. In 2D flows, transition criteria may be expressed using functions that are quite insensitive to this. It is not so in 3D, because characteristics of the velocity profile in the vicinity of its inflection point plays a major role on stability. It was thus decided that boundary layer codes were necessary tools in order to guarantee the requested precision. The mean flow pressure distribution was provided by turbulent RANS computations. The choice of fully turbulent flow improves the convergence rate while producing essentially the same pressure distribution as a computation with prescribed transition.

Validation was based on comparisons to a reference experiment, which took place in the ONERA F1 wind tunnel at the end of 2000 and was in itself a task in EUROLIFT. The model used, called AFV, is a three element swept wing with a constant chord of 0·5m, see Fig. 19. Two values of sweep, 30° and 40°, were used. Transition observations were obtained for chord Reynolds numbers between $1{\cdot}5 \times 10^6$ and 10×10^6. Description of the experiment, with major findings explained, has been presented in Ref. 16.

4.2 Contamination

Attachment line contamination is due to the transport of fuselage turbulence along the attachment line of the wing. Increased sweep and large wing radius in the leading-edge region promote this transport. When this occurs, the whole wing surface becomes turbulent, with no laminar region. Attachment line contamination is characterised by the parameter:

$$\bar{R} = W_e \Big/ \sqrt{\nu \left(\frac{\partial U_e}{\partial X} \right)_{X_a}} \qquad \ldots (1)$$

with X_a referring to the attachment line, which can be written in case

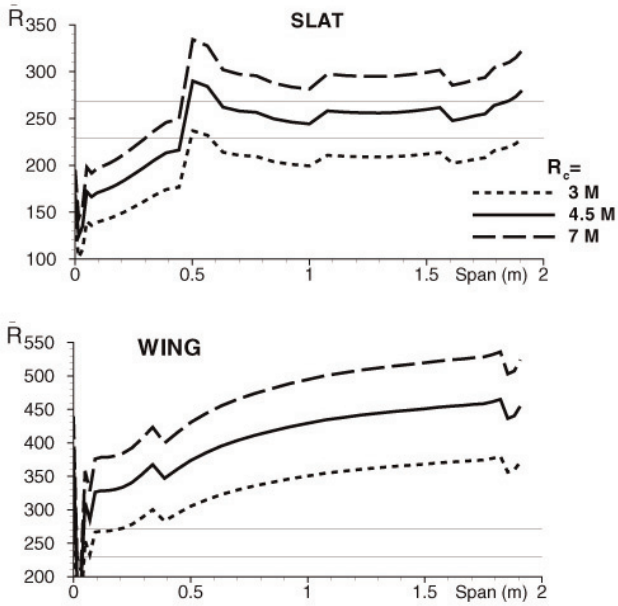


Figure 20. Spanwise evolution of the contamination Reynolds number (φ = 40°, α =10°).

of a swept cylinder of radius R in a flow of velocity Q_{inf} as:

$$\bar{R} = \sqrt{\frac{Q_{inf}\mathbf{R}}{\nu}} \sqrt{\frac{1}{2}\mathrm{Sin}\varphi\mathrm{Tan}\varphi} \qquad \ldots (2)$$

thus increasing as the square root of the Reynolds number, or of the nose radius. Critical value of this parameter is usually taken as 250 ± 20[17]. It can be computed in the pre-processing phase, together with the effective sweep angle. Figure 20 shows typical evolutions obtained on the slat and the main wing of the AFV model, showing that the main wing should always be contaminated at 40° sweep and the slat at large Reynolds numbers. The flap, not presented, is never contaminated. These predictions were verified in the experiment.

4.3 Transition prediction tools

The database method used for transition prediction allows, with high efficiency, an estimation of the stability characteristics of 3D boundary layers. Growth rates obtained are integrated to produce N-factors exactly as in case of exact stability theory[18]. The N-factor is usually obtained using the envelope strategy. In this case, stationary disturbances (usually not the most amplified) are eliminated from the computation. Two models are used, one for longitudinal instabilities, and the other for progressive crossflow ones. In both case, it is assumed that the Reynolds number variation of the exact growth rate, obtained solving the Orr-Sommerfeld equations for a given profile, can be expressed using two half parabolas, Fig. 21:

$$\sigma = \sigma_M \left(1 - \left(\frac{R_{\delta_1} - R_M}{R_k - R_M} \right)^2 \right) \qquad \begin{array}{l} R_k = R_0 \; if \; R_{\delta_1} < R_M \\ R_k = R_1 \; if \; R_{\delta_1} > R_M \end{array} \qquad \ldots (3)$$

Hence, the parabola model requires determination of four parameters R_0, R_1, R_M, σ_M, where σ represents the growth rate, as function of frequenc $F = \frac{2\pi f \nu}{U_e^2}$, local flow conditions and boundary layer characteristics. The longitudinal model is based on a lookup table, using the incompressible shape factor H_i and the local Mach number as parameters. The cross-flow model is based on a more

https://doi.org/10.1017/S0001924000000555 Published online by Cambridge University Press

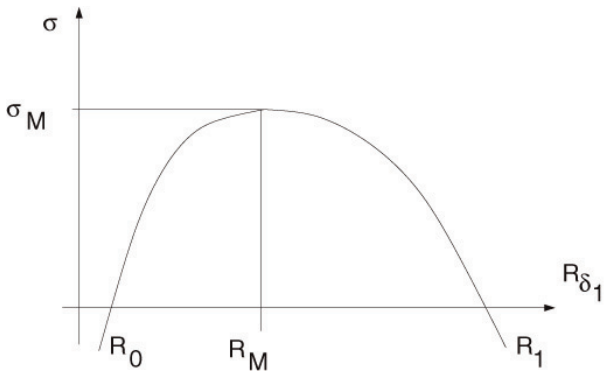


Figure 21. Growth rate variations represented using parabolas.

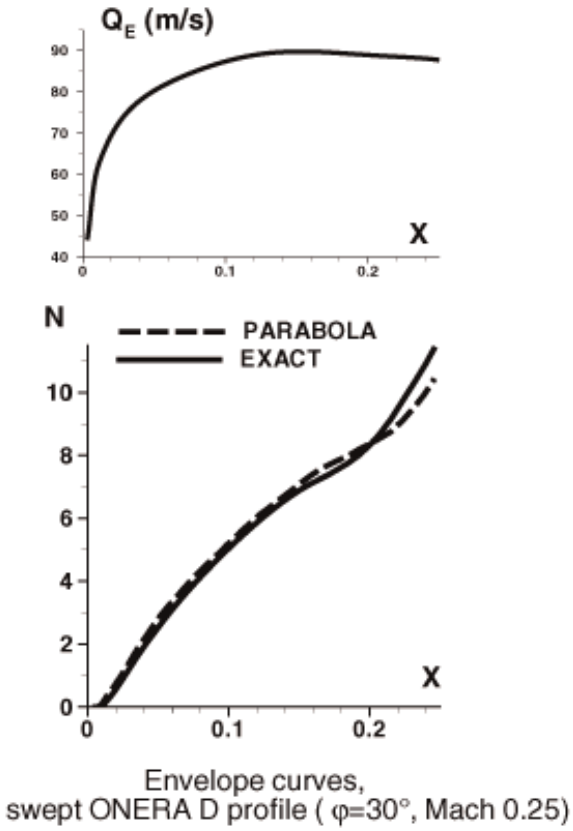


Figure 22. Database validation on a swept case.

complex analytical formulation, depending on the characteristics of the inflection point $U(y_i)$ and $P_i = y_i \left(\frac{\partial U}{\partial y}\right)_i$, where y_i is the height of the inflection point in the velocity profile. If several inflection points appear usually the highest inflection point is taken. In case of 3D boundary layers, the amplification in any direction j is computed from the 2D profile obtained by projection in that direction of the 3D velocity profile, using Stuart's theorem[19] and Gaster's relation[20]. Careful optimisation has ensured that, in general, the most amplified frequencies are represented with a precision of about 1 count in N-factor.

One important advantage of the method is that it does not require any initial values.

It was first decided to validate partners' implementation of the simplified method into their own boundary layer codes, using a common 3D boundary layer around the same ONERA D profile in swept wing configuration ($\varphi = 30°$, M = 0·25, Rc = 1·75 × 10⁶, α = –6º). Input data was the pressure distribution and not the boundary layer profiles. Fig. 22 shows a comparison of exact local stability results compared to database results. Partners obtained similar results in this case.

4.4 Short bubble transition

In many high lift cases, transition to turbulence occurs through laminar separation, due to strong positive pressure gradients. Such regions of decelerated flow are always strongly unstable, as well as separated regions, through longitudinal instabilities. The large amplifications may cause transition to occur shortly after, if not before, separation. Although the physical aspects are strongly linked, separation is usually detected in the course of the boundary layer computation, hence independently of stability calculations. After testing if a turbulent solution can be accepted, the code may then proceed assuming turbulent flow, hence a zero length separated region, or otherwise stops. Physically, the separated 'bubble' should have a non-zero length. In the experiment, hot films did detect turbulent flow upstream of reattachment line, well visible on the infrared images. Rapid boundary layer growth needs to be accounted for in this region. This problem of transition in a separated flow is not fully solved up to this day.

4.5 Relaminarisation

The acceleration parameter

$$K = \frac{\nu}{U_e^2}\frac{\partial U_e}{\partial x} \qquad \ldots (3)$$

proposed by Beasley for 2D flow[21] is a local parameter, independent of boundary layer parameters, which can be computed in the pre-processing step together with attachment line transition indicator $\bar{R}$. In 3D flow, K should be evaluated in the streamline direction. Relaminarisation of a turbulent boundary layer should be expected if values of K are larger than 5×10^{-6} over a significant distance. Large values have the effect of keeping the boundary layer in a quasi laminar state, called 'laminarescent'[22], but as soon as K decreases the turbulence reappears rapidly. Return to turbulence proceeds as in a 'bypass' transition, without going again through a linear stage. A turbulent flow is required upstream of relaminarisation, as may be caused by contamination.

Occurrences of partial relaminarisation were observed in the experiment, causing sharp reduction in velocity fluctuations. Values of K were indeed close to 5×10^6.

4.6 Application to the AFV experiment

Although all three elements of the wing were considered in the course of the project, only results for the upper slat element will be presented here. The upper slat was well equipped and observed by the infrared camera. With varying incidence and Reynolds number, every mentioned phenomenon were observed on this element, transition and contamination at low incidences, and, at large incidence, separation and partial relaminarisation. Turbulent RANS computation, using the elsA code of ONERA with a *k*–l Smith turbulence model provided the pressure distributions over the model. 2·5D theory was then used to generate the velocity distributions, assuming

https://doi.org/10.1017/S0001924000000555 Published online by Cambridge University Press

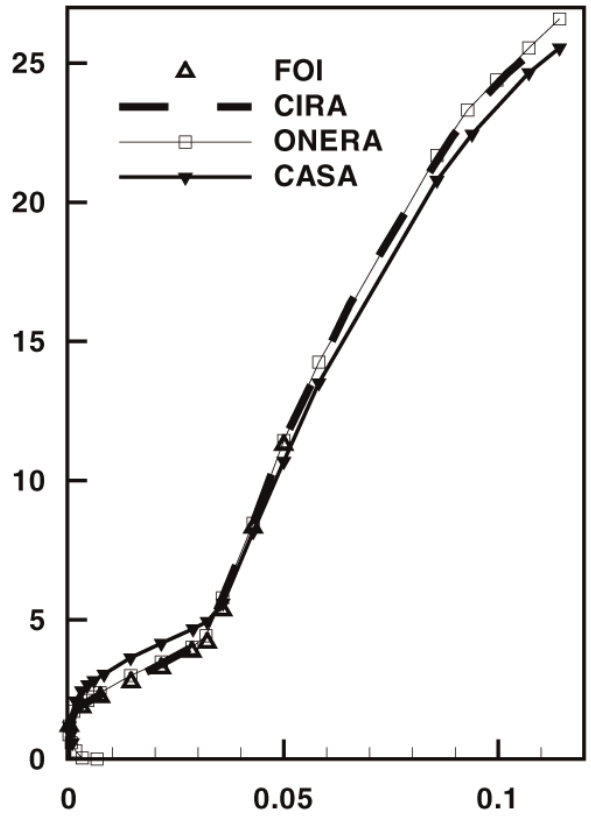


Figure 23. Database N-factor curves for a typical upper slat case, comparing partner's results.

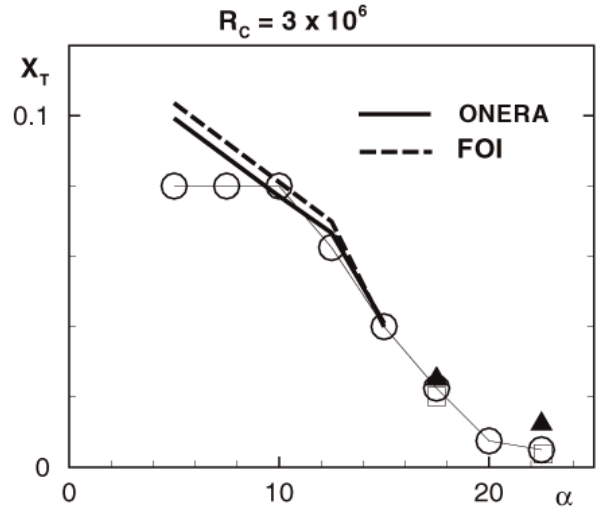


Figure 24. Upper slat transition evolution. Circles for experimental results, lines and symbols for numerical results. Triangles and squares for separation, lines for transition predictions.

a constant spanwise velocity component W_e. Then, task partners used their own boundary layer codes with the integrated simplified stability method, to predict transition.

Fig. 23 shows a typical result, comparing *N*-factor curves from four partners for a case that is clearly cross flow at the start, then becomes longitudinal past the strong pressure gradient. This is observed at 40° sweep, 15° incidence and a chord Reynolds number of 3×10^6. For the same sweep angle and Reynolds number, Fig. 24 shows the predicted transition evolution obtained by FOI and ONERA, compared to the experimental results. The numerical results are represented with lines for transition predictions, and symbols for separation.

At 5° incidence, transition is of TS type and is not well predicted: the relative error is close to 20%. Between 5° and 10°, both TS and CF instabilities exist, and prediction gradually improves. Then, between 10° and 15°, the CF transition is very well predicted. Above 15°, the computation method indicates flow separation with short bubble transition, which is correctly predicted.

A more detailed presentation of the AFV transition studies is available in Ref. 22.

5.0 CONCLUSION

Main achievements of the numerical work package of the EUROLIFT high lift program are described. Concerning CFD assessment a first common computation of a simplified 3D high lift aircraft configuration is accomplished. Maximum lift is simulated in fair agreement to the experimental evidence for wind tunnel conditions. Nevertheless, a considerable scatter of the results of a variety of European codes is observed, especially with respect to the drag determination. The simulation quality of block-structured and unstructured grid methods is comparable. To increase the reliability of the 3D maximum lift simulation, further investigations on high resolution grids are needed. The industrial use of such simulations clearly requires improvements of accuracy, efficiency, and a transition prediction capability for 3D configurations in the RANS methods.

The improvement activities demonstrate that features such as the preconditioning technique and efficient grid generation approaches hold promise to cope with the aforementioned requirements. For high lift flows, the EARSM extension of the eddy viscosity turbulence models has been shown not to offer the benefits observed in transonic applications. Thus, appropriate turbulence modelling of strongly separated flows remains a challenge pointing at more advanced physical modelling, as e.g. detached eddy simulation (DES) concepts.

Transition work was very active during the entire EUROLIFT project, and significant progress was achieved, both in the physical understanding of high lift transition phenomena and in the validation of fast database prediction methods.

The simplified stability analysis provided with the database method proves quite adequate for high lift flows, although the simplified method cannot represent perfectly all cases. On the other hand, the database method is capable of computing reasonable amplification rates in cases where local methods require lots of time and efforts. Relaminarisation is an important issue in wind tunnel tests, while its effect should be small at flight Reynolds numbers. Attachment line contamination, on the contrary, should be generally expected at flight Reynolds numbers. Transition through separation remains difficult to model. In RANS approaches, separation may be represented but transition cannot be yet predicted in the separated region. Obviously, progress is needed on that topic.

ACKNOWLEDGEMENT

The investigations presented in this paper have been obtained within the European research project EUROLIFT under contract No G4RD-CT-1999-00072, which is funded by the EC in the Fifth framework programme 'Promoting Competitive and Sustainable Growth'. The authors are grateful to the EUROLIFT partners for providing the results discussed in the paper.

https://doi.org/10.1017/S0001924000000555 Published online by Cambridge University Press

REFERENCES

1. RUMSEY, L.R. and YING, S.X. Prediction of high lift: review of present CFD capability, *Prog in Aerospace Sci*, 2002, **38**, pp 145-180.
2. LINDBLAD, I.A.A. and DE COCK, K.M.J. CFD Prediction of maximum lift of a 2D high lift configuration, 1999, AIAA-99-3180.
3. THIBERT, J.J. The GARTEUR high lift research programme, AGARD-CP-515 High Lift System Aerodynamics, 1993, pp 16-1 - 16-21.
4. THIEDE, P. EUROLIFT — advanced high lift aerodynamics for transport aircraft, *Air & Space Europe*, 2001, **3**, (3/4), pp 1-4.
5. RUDNIK, R. Towards CFD validation for 3D high lift flows — EUROLIFT, 2001, European Congress on Computational Methods in Applied Science and Engineering, ECCOMAS conference proceedings, IMA, ISBN 0 905 091 124 (CD-ROM), pp 1-20.
6. SCHWARZ, T. Development of a wall treatment for Navier-Stokes computations using the overset-grid technique, 200, Paper No 45, Proceedings of the 26th European Rotorcraft Forum, 26-29 September 2000, The Hague, The Netherlands.
7. EDWARDS, J.R. and CHANDRA, S. Comparison of eddy viscosity-transport turbulence models for three-dimensional shock separated flowfields, *AIAA J*, April 1996, **4**.
8. WALLIN, S. and JOHANSSON, A.V. An explicit algebraic Reynolds stress model for incompressible and compressible turbulent flows, *J Fluid Mech*, 2000, **403**, pp 89-132.
9. ELIASSON, P. CFD Improvements for high lift flows in the European project EUROLIFT, 2003, AIAA-2003-3795, Orlando, FL, USA.
10. HANSEN, H. and SZABO, I. Investigation of stall characteristics of an A3XX relevant airfoil up to high Reynolds numbers in the technology Program HAK 2, *Notes on Numerical Fluid Mechanics*, 1999, **72**, Vieweg Braunschweig.
11. RUDNIK, R. Common European CFD-code validation for complex high lift configurations — the challenge of coming from observations to conclusions, 2002, DGLR Jahrestagung, Stuttgart, Germany, *DGLR-Jahrbuch 2002*, Bd III, JT 2002-015.
12. CHOI, Y.H. and MERKLE, C.L. The application of preconditioning to viscous flows, *J Computational Physics*, 1993, **105**, pp 207-223.
13. WEISS, J.M. and SMITH, W.A. Preconditioning applied to variable and constant density flows, *AIAA J*, 1995, **33**, (11), pp 2050-2057.
14. ARNAL, D. Transition prediction in transonic flows, 1988, ZIEREP and OERTEL (Eds), IUTAM Transsonicum III Symp, Göttingen.
15. CASALIS, G. and ARNAL, D. Database method — development and validation of the simplified method for pure crossflow instability at low speed 1996, ELFIN II Tech Rep N° 145.
16. SÉRAUDIE A., PERRAUD, J. and MOENS, F. Transition measurement and analysis on a swept wing in high lift configuration, December 2003, *AST*, **7**, (8), pp 569-576.
17. PFENNINGER, W. Flow phenomena at the leading edge of swept wings, *Recent Dev in Boundary Layer Research*, 1965, AGARDograph 97.
18. SMITH, A.M.O. and GAMBERONI, N. Transition, pressure gradient and stability theory, 1956, Douglas Aircraft Co, Rept ES 26388, El Segundo, CA, USA.
19. GREGORY, N., STUART, J.T. and WALKER, W.S. On the stability of three dimensional boundary layer with application to the flow due to a rotating disc, *Philosophical Transaction of the Royal Society of London*, 1955, A 248, pp 155-199, London, UK.
20. GASTER, M. A note on the relation between temporally increasing and spatially increasing disturbances in hydrodynamic stability, *J Fluid Mechanics*, 1962, **14**, pp 222-224.
21. BEASLEY, J.A. Calculation of the laminar boundary layer and prediction of transition on a sheared wing, 1976, RAE Farnborough Rep N° 3787.
22. ARNAL, D. and JUILLEN, J.C. Leading edge contamination and relaminarisation on a swept wing at incidence, 1989, Fourth Symposium on Numerical and Physical Aspects of Aerodynamics Flows, Calif State Univ.

https://doi.org/10.1017/S0001924000000555 Published online by Cambridge University Press